



OPEN

Model experimental study on the mechanism of collapse induced by leakage of underground pipeline

Jixiang Guo^{1,2}, Yanjun Zhang^{1,2}✉, Yunfeng Li³, Xin Zhang¹, Jianqiao Zheng¹, Haoxin Shi¹, Qing Zhang³, Zongfang Chen³ & Yongjie Ma⁴

The evolution and mechanism of ground collapse caused by underground water pipeline leakage have become increasingly significant as more urban areas experience collapses. Based on the principle of similarity, and considering the engineering context of road collapses in Anqing City, Anhui Province, this study designed a 3 m × 2 m × 2 m rupture-collapse model test device. Digital Image Correlation (DIC) technology was employed to investigate the erosion process and collapse mechanisms caused by underground pipeline leakage. The results indicate that groundwater seepage provides the driving force for collapses, combined with the migration space provided by defects, collectively triggering the collapses. When groundwater seepage is minimal, the cohesive forces between soil particles maintain soil stability. As groundwater seepage increases, the soil particle framework is eroded, leading to soil structure destabilization and collapse initiation. The depth of collapse significantly influences stress evolution: stress evolution intensity beneath and above the collapse pit is positively correlated with the distance from the collapse pit bottom, but negatively correlated with the distance from the defect. The research provides insights for the early warning and management of ground collapse.

Keywords Underground space, Pipeline leakage, Collapse mechanism, Groundwater, Physical model test

In recent years, urban underground spaces have been increasingly affected by human activities such as the construction of underground infrastructure, pipeline construction, and heavy traffic, leading to frequent subsidence incidents^{1,2}. Urban ground collapse incidents are characterized by their hidden and sudden nature, making them difficult to predict with existing monitoring systems³. Consequently, such incidents are increasingly being reported in many cities, including those in Canada⁴, Indonesia⁵, and Iran⁶. With the rapid development of urbanization in China, the high load of municipal pipelines and road traffic has led to a large number of collapse accidents nationwide every year (Fig. 1)⁷. Wang and Xu⁸ summarized and analyzed the collapse accidents occurred in China and found the underground pipeline leakage⁹, rainfall, underground engineering and geological conditions are the main causes of urban ground collapse. Among them, underground pipeline leakage accounts for more than 40%. When the buried pipeline leaks, the sand and water around the pipeline migrate into the pipeline and are washed away, forming a cavity in the strata, resulting in changes in the stability of the stratum near the pipeline. Eventually, as the cavity expands, the overlying soil becomes unstable¹⁰, resulting in collapse. The current research mainly focuses on the influencing factors of pipeline leakage and the estimation of seepage rate through its mechanical behavior, etc., but neglects the research of soil erosion mechanism, which is an important process to prevent urban ground collapse. Therefore, it is of great significance to study the process of ground collapse caused by pipeline leakage and explore the mechanism of soil–water interaction for urban disaster prevention and safety.

At present, theoretical methods^{11–20}, numerical simulations^{21–30} and physical model tests have been adopted for the stability analysis of ground collapse caused by pipeline leakage. Physical model tests have the advantages of being realistic, intuitive, and scientific, which have been widely applied in the field of geotechnical engineering^{31–35} and have achieved remarkable research results in collapse. For example, Sato and Kuwano³⁶

¹College of Construction Engineering, Jilin University, Changchun 130026, China. ²Key Lab of Groundwater Resource and Environment, Ministry of Education, Jilin University, Changchun 130026, China. ³Nanjing Center, China Geological Survey, Nanjing 210016, China. ⁴Zhejiang Huadong Geotechnical Investigation & Design Institute Co., Ltd, Hangzhou 310023, China. ✉email: zhangyanj@jlu.edu.cn

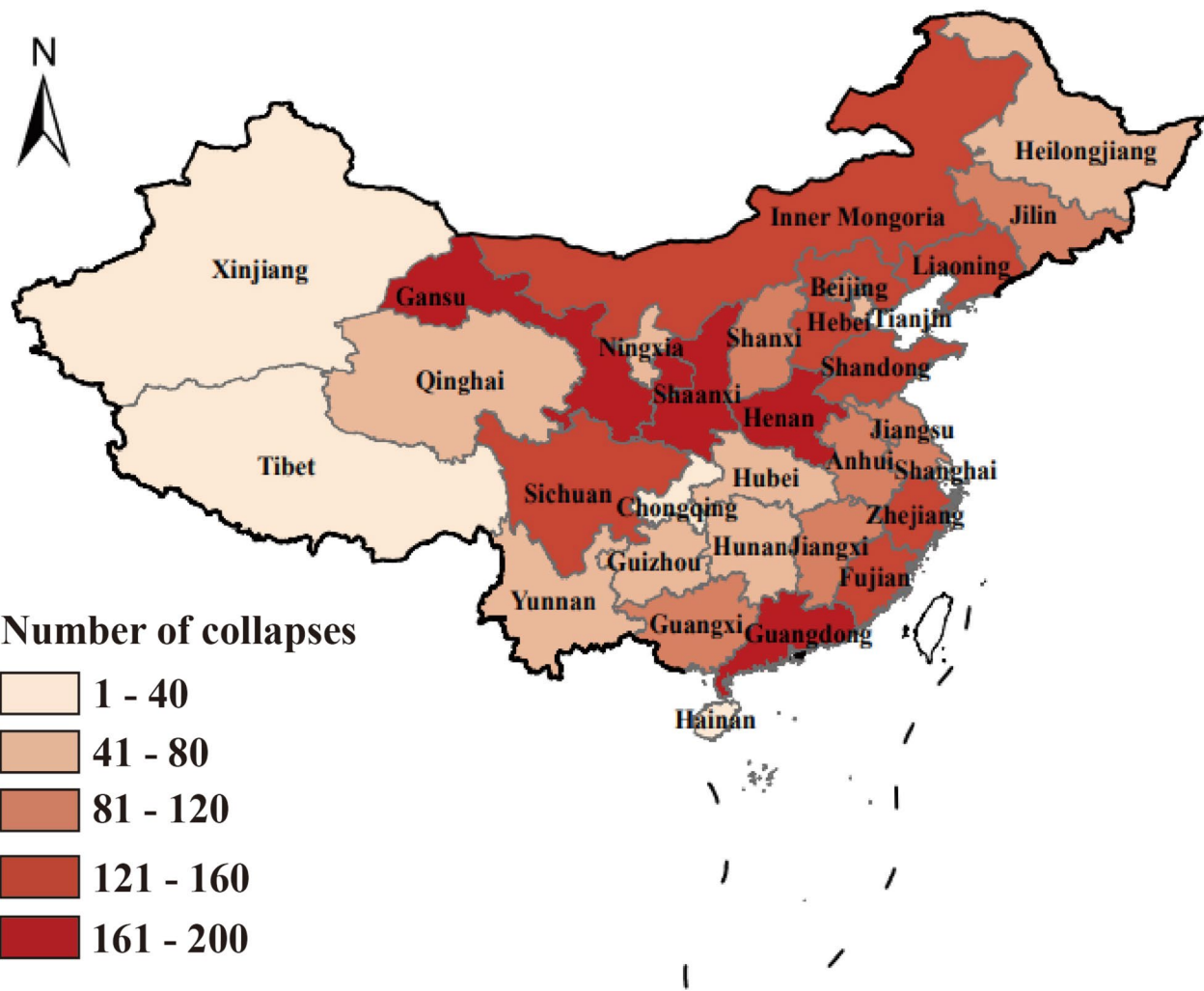


Figure 1. Distribution of urban ground collapse in China (adapted from Wang and Xu⁸). The map was generated using Adobe Illustrator 2021, Illustrator Free Download & Free Trial|Adobe Illustrator.

conducted model tests to examine the correlation between pipeline leakage and underground cavity expansion. Zhang et al.³⁷ used plane strain model tests to investigate the influence of shallow tunnel pipeline leakage on foundation collapse, which showed that pipeline leakage caused the overlying soil no longer had sufficient support, resulting in collapse. Guo et al.³⁸ and Cui et al.³⁹ analyzed the effects of defect size, groundwater, and particle grade on seepage damage. Sato and Kuwano⁴⁰, Mukunoki et al.⁴¹ and Indiketiya et al.³⁴ analyzed the pipeline leakage in sandy soils and found that particles smaller than 0.3 mm are very easy to be eroded in 5 mm defect, which indicates that the soil of cavities is related to the loss of soil particles and the soil accumulation density around the defect. Ahmed Ibrahimp²² investigated the effect of groundwater table, defect size, defect angle and height of sand fill above the pipeline on erosion by means of a coupled hydrodynamic-discrete element approach.

The results of these studies indicate that physical model tests are an effective means of reproducing the process of ground collapse caused by the pipeline leakage. The urban ground collapse caused by the pipeline leakage mainly depends on the particle size, defect characteristics, soil height and groundwater conditions. However, little research has been reported on the use of physical model tests to investigate the soil erosion process of collapse caused by pipeline leakage and the mechanism of soil–water interaction. Tan and Lu⁴² studied the damage of buried pipelines, groundwater seepage from the defect takes away a large amount of soil, which leads to the emergence of cavities, but did not have a deeper understanding of the damage process. Meanwhile, Wang et al.⁴³ and Tan et al.⁴⁴ used model tests to reveal that seepage has an important role in the collapse process, and found that vertical damage has the greatest influence on the development of cavities and ground collapse. Nevertheless, they did not uncover the intrinsic soil–water interaction mechanism. These studies have some insights into the resilience evaluation of urban underground pipeline leakage. It should be noted that most of such studies are based on small-size models or two-dimensional model tests with a single direction of seepage, and it is doubtful to what extent they are similar to the real conditions of pipeline leakage leading to collapse. And there are fewer

studies on the soil erosion response process and mechanism of action in the collapse caused by pipeline leakage, which leads to frequent urban collapse accidents.

Different from the previous research, this paper designs a $3\text{ m} \times 2\text{ m} \times 2\text{ m}$ pipeline leakage leading to collapse model test device based on the similarity theorem. DIC technology and numerous high-precision pressure sensors are applied to study the internal response process and mechanism of soil erosion by pipeline leakage. The process of ground collapse caused by pipeline leakage was simulated by experiments, and the evolution law of stress in different strata and the law of groundwater erosion were analyzed; based on the DIC technology, the effects of soil erosion process and the morphology development characteristics of the collapse pit on the collapse were studied. Combining these results, it was confirmed that groundwater provides the driving force for the collapse caused by pipeline leakage, and the defective pipeline provides the transportation space for this process. This study lays a theoretical foundation for the resilience assessment of urban underground pipelines and the development of new technologies for monitoring and early warning of such disasters in underground spaces.

Design of model test

Engineering background

The area along the Yangtze River in Anqing City is located in the flood area of the Quaternary Yangtze River alluvial plain, the thickness of the overburden layer is 30–60 m, the lower part is Cretaceous sandstone, the submerged water table depth is 0.5~2.0 m, and the pressurized water table depth is 0~6 m. The riverfront area primarily features two sand layers, with a central layer of plastic silty clay. The buried depth of the top plate first layer is 0.7~5.7 m, the buried depth of the bottom is 3.25~18.4 m, and the thickness is 1.95~16.5 m; the buried depth of the top plate of the second layer is 20.0~34.45 m, the buried depth of the bottom plate is 31.0~38.65 m, and the thickness is 4.2~11.0 m. In February 2019, a collapse occurred on the central section of Changfeng Road in Yingjiang District, Anqing City, covering an area of approximately 30 m^2 with a depth of nearly 1.5 m, as shown in Fig. 2. The collapse caused the surrounding road surface to become "suspended", exposing the roadbed and other underlying structures, and severely tilting the sidewalk trees. The collapsed section is located within the Yangtze River alluvial floodplain zone, with a sewage pipeline installed within it. It was observed that the

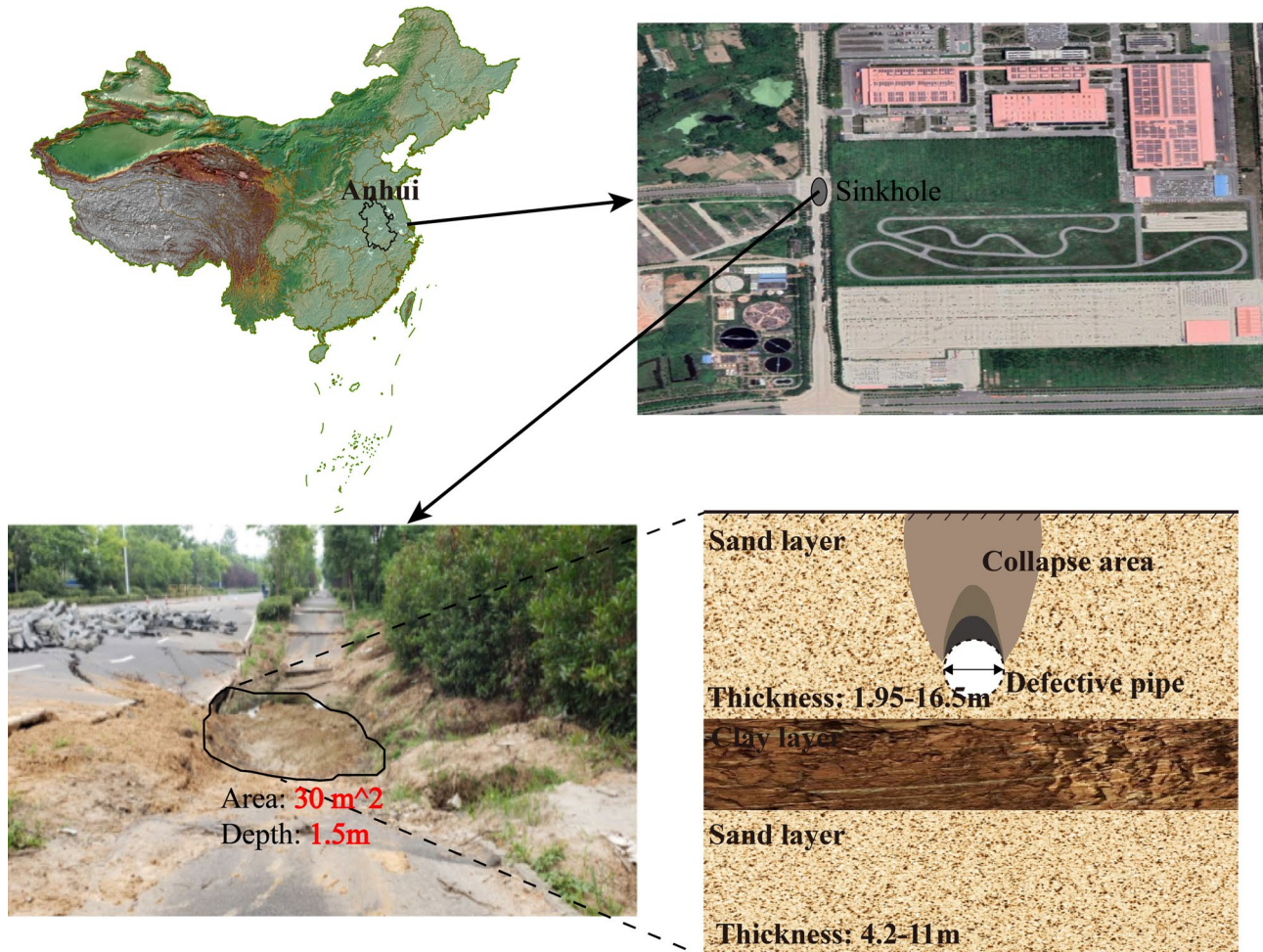


Figure 2. Location and stratigraphic information of the collapse area. The map was generated using Adobe Illustrator 2021, Illustrator Free Download & Free Trial | Adobe Illustrator. The satellite imagery was generated using Google Earth Pro7.3.6, Google Earth.

sewage pipeline was placed in the bad sediment in the diffuse beach area, and the excavation depth of the sewage pipeline at the collapsed section was about 8 m, mainly distributed in the sand layer, and covered with 1.5 m of artificial fill in the upper part of the sand layer. According to investigations by relevant authorities, the cause of the incident was a leak in the shallow sewage treatment pipeline, which created a pressure difference between the inside and outside of the pipe. Groundwater carried away the fine sand beneath the road surface, resulting in the road surface being unsupported and ultimately collapsing.

Physical model test system

In this study, an independently designed collapse simulation platform was used to carry out the simulation test of underground pipeline leakage and collapse. The simulation test device mainly consists of four parts: model box system, flow control system, leakage sedimentation system, and monitoring system, as shown in Fig. 3.

As described in Section "Engineering background", the buried depth of the ground collapse underground drainage pipeline in Anqing City was about 8 m. The geometric similarity ratio of the model test is 1:10, and considering the thickness of the pipeline, the diameter (D) and the buried depth (L) of the drainage pipeline in the model test are 10 cm and 80 cm in the model test respectively. To account for the influence of self-weight stress fields, the gravity similarity ratio in the model test is 1, matching the field conditions. The design of the model box is shown in Fig. 4. The model box is made of Q235 steel plates with 6 mm thick sides and 8 mm thick bottom, and high strength bolts are used to connect the parts. The overall dimensions of the model box are $3\text{ m} \times 2\text{ m} \times 2\text{ m}$,

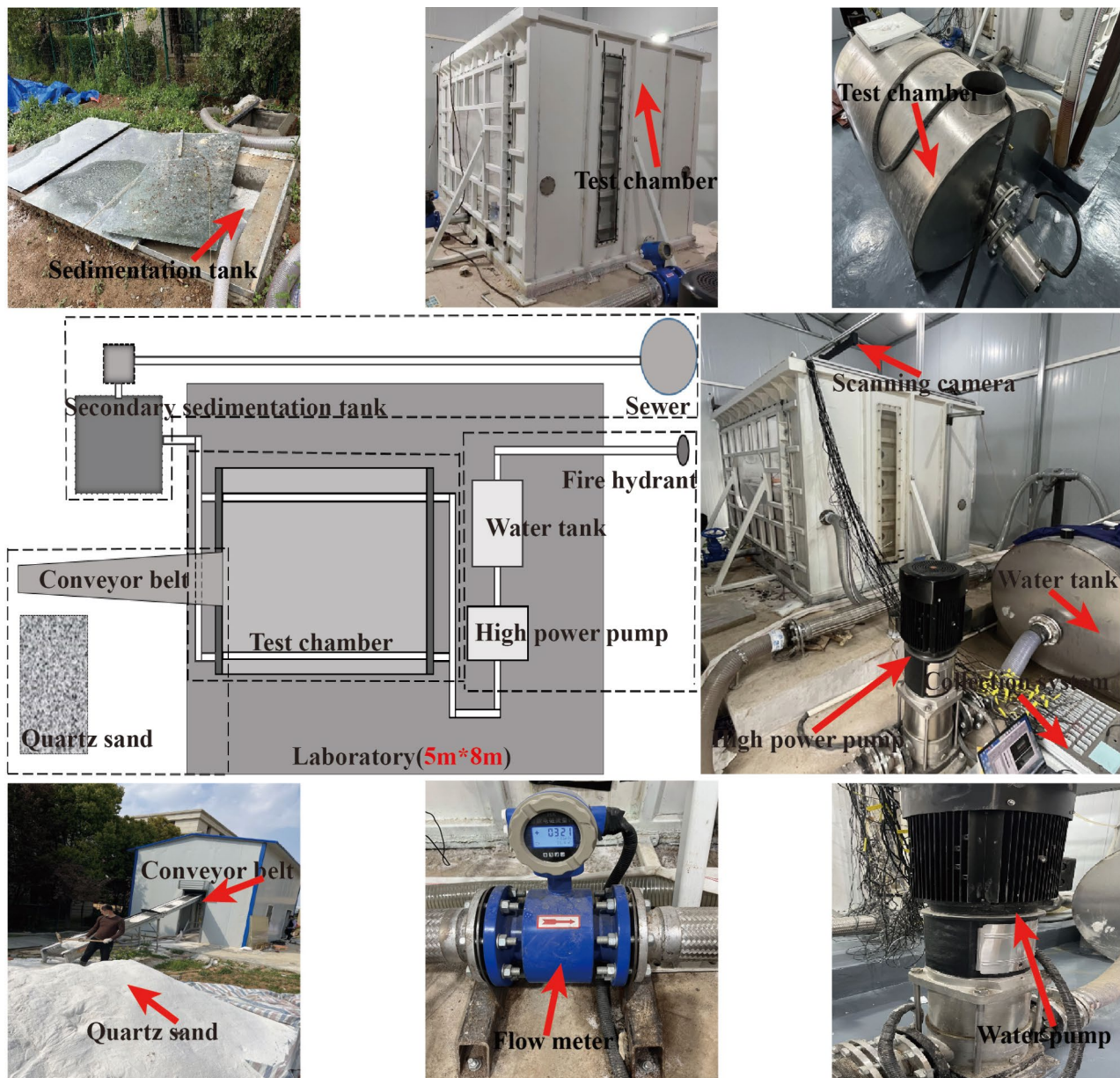


Figure 3. Physical model test system.

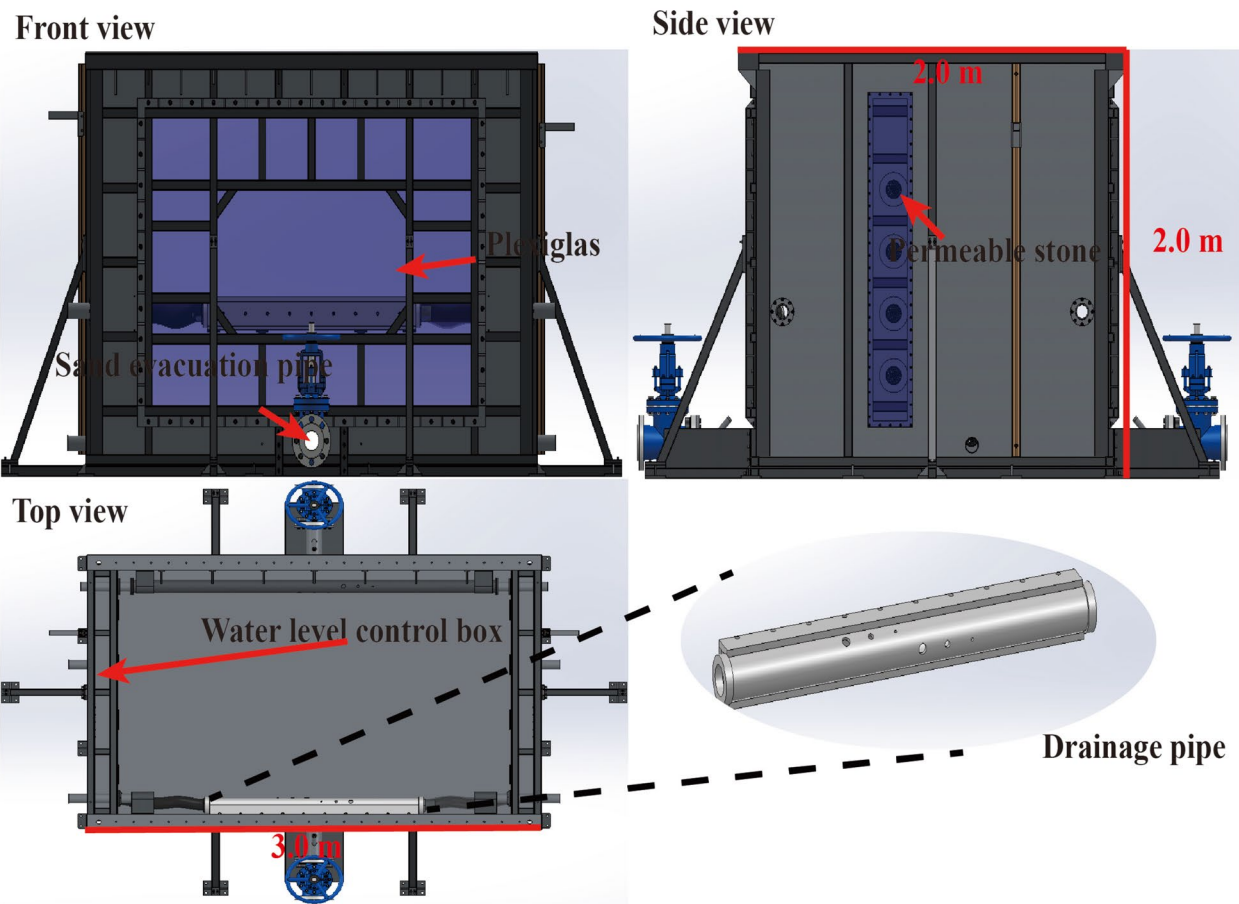


Figure 4. Model box design information.

with observation windows made of 2 cm thick plexiglass at the front and rear to monitor internal erosion and settlement. Water level control boxes are installed on both sides of the model box, measuring $2\text{ m} \times 0.2\text{ m} \times 2\text{ m}$. The inside of the water level control boxes are equipped with 40 permeable dividers of 10 cm in diameter to ensure that it is difficult for the sand to pass through. Zoueshtiagh and Merlen⁴⁵ pointed out that the change of the diameter of the orifice has no effect on the critical flow rate of the full fluidization of the soil damage when the leakage loss is upward through the experiments. Inside the model box, a 10 cm diameter plexiglass pipeline is installed, with a 20 mm circular defect located above the middle of the pipeline. The flow control system in the test has a maximum flow rate of $42\text{ m}^3/\text{h}$ and a head of 40 m; the leakage sedimentation system mainly separates water and sand through a sedimentation tank; the monitoring system consists of a DIC monitoring system and a pressure sensor system, and the working principle is shown in Fig. 5.

Test schemes and procedures

In this test, approximately 30 tons of quartz sand has been used as the test material to reduce the influence of impurities. During the test, the collapse displacement in stratum was captured by a visual displacement analyzer (Fig. 5) with a resolution of 1200 w. The displacement measurement accuracy can reach 0.01 mm, and three photos can be taken per second to record the collapse process. The changes in soil pressure were tracked using DMTY strain-type soil pressure sensors (Fig. 5), which have a measuring range of 0.05–10 MPa and a measurement accuracy of $\leq 0.5\%$ F.S. The main steps of the test were as follows:

1. Selection of similar devices. According to the similarity ratio of 1:10 in the model test, a Plexiglas drainage pipeline with a diameter of 10 cm, a height of 79.3 cm, a depth of 80 cm from the ground, and a circular defect with a diameter of 20 mm were selected as the defect during the test. A 10 cm diameter gold wire hose was used to connect each system within the test.
2. Sand filling and sensor layout. The quartz sand was transported into the model box through the conveyor belt, and then the quartz sand was compacted manually using a wooden hammer. The compaction in stratum is shown in Table 1. During sand filling, once a certain depth is reached, corresponding pressure sensors need to be put into it. The distribution location in stratum of the soil pressure sensor is shown in Table 2, where X indicates the distance from the sensor to the plexiglass plate, Y indicates the distance from the sensor to the short side of the model, and Z indicates the distance from the sensor to the bottom of the model box. Finally, after allowing the entire system to stand still for 24 h, water is introduced until the water level reaches

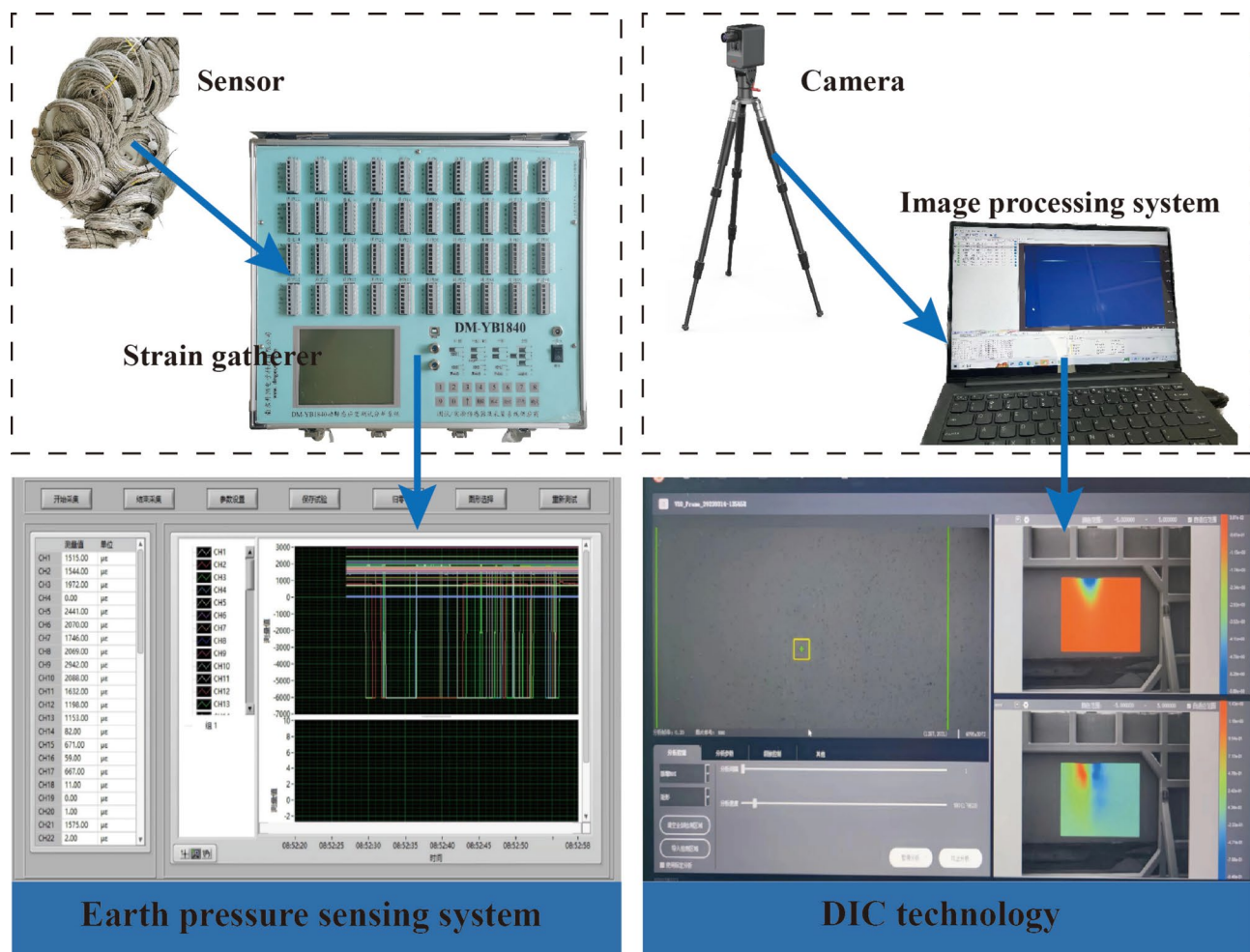


Figure 5. Monitoring system.

Layer	Height before compaction/cm	Height after compaction/cm	Number of sensors
1	22.8	20.5	0
2	40.7	39.0	0
3	62.7	60.5	2
4	81.5	79.3	4
5	89.7	88.6	4
6	110.3	107.5	4
7	128.0	126.5	7
8	146.0	144.7	6
9	162.0	159.3	0

Table 1. Ground compaction information and number of sensors.

150 cm. Another 24 h static period follows to minimize the influence of pre-testing creep effects as much as possible. Throughout the test, the water level height is maintained constant using a water table control box.

3. Pipeline leakage. A 20 mm circular defect appeared by removing the rubber plug inside the plexiglass tube. At the beginning of the test, the flow rate of water in the pipeline was controlled to be $2\text{m}^3/\text{s}$. The water did not make the pipeline full, and it also prevented the sand that had leaked from the defect location from accumulating in the pipeline. At the end of the test it could be observed that the collapse in the model box did not change, only water flowed out of the pipe, and no new sand particles appeared in the settling tank.

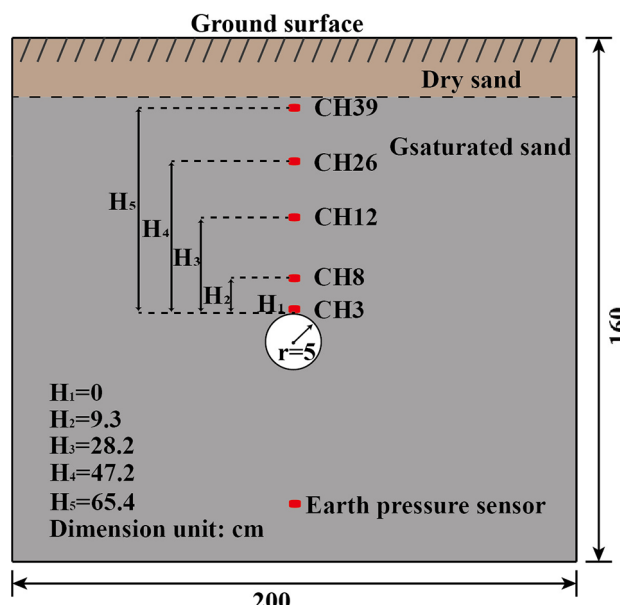
Name of Sensor	Basic parameter Kpa/ $\mu\text{\xi}$	X/cm	Y/cm	Z/cm
CH3	0.06944	18	120	79.3
CH5	0.0885	18	106	79.3
CH6	0.0901	18	134	79.3
CH7	0.05291	34	120	79.3
CH8	0.09259	18	120	88.6
CH9	0.08	18	100	88.6
CH10	0.09091	18	140	88.6
CH11	0.09009	38	120	88.6
CH12	0.07813	18	120	107.5
CH13	0.07813	18	95	107.5
CH21	0.07874	18	145	107.5
CH25	0.09524	43	120	107.5
CH26	0.06757	18	120	126.5
CH27	0.0625	18	95	126.5
CH28	0.06803	43	120	126.5
CH29	0.012107	18	80	126.5
CH30	0.01111	58	120	126.5
CH31	0.09615	18	145	126.5
CH34	0.07692	18	160	126.5
CH35	0.06667	68	120	144.7
CH36	0.01066	43	120	144.7
CH37	0.06897	18	70	144.7
CH38	0.06452	18	170	144.7
CH39	0.0641	18	120	144.7
CH40	0.0885	18	95	144.7

Table 2. Sensor parameters and position.

Model test results and discussion

Analysis and discussion of stress evolution in the vertical direction

The distribution of vertical pressure sensors is shown in Fig. 6, with distances from the pipeline defect positions of 0 cm, 9.3 cm, 28.2 cm, 47.2 cm, and 65.4 cm, respectively. The acquisition frequency of the pressure sensor was set to 40 times per second during the test, with data collection starting from the moment the water pump

**Figure 6.** Vertical sensors distribution.

initiates collapse. The test lasted for 2648 s, and each soil pressure sensor obtained 105,920 data. To facilitate data analysis, the average value of stress per second was taken. The evolution of vertical stresses in the strata during the test is shown in Fig. 7. Based on the test results, the evolution process is divided into three stages: the first stage where seepage failed to erode the strata, known as the initial stage; the second stage where the soil particle skeleton of the strata was eroded, known as the erosion stage; and the third stage where collapse development gradually stabilized, known as the stable stage.

In the initial stage, the stress evolution at positions H_1 , H_2 , H_3 , H_4 , and H_5 in the vertical direction is generally consistent. As shown in the left diagram of Fig. 7, the stress evolution curve is convex-shaped with relatively small variations in stress magnitude. At the H_1 measurement point, the longest stress evolution time is 278 s, with the maximum variation being 0.18 kPa. Assuming the internal particles of the soil are spherical and under the same stress conditions, when the pipeline leakage initially occurs, the seepage force formed during the leakage process are insufficient to cause damage to the soil skeleton, thus the soil remains stable. However, the seepage force acting on the finer particles inside exceed their maximum restraint force, causing these finer particles to erode along the soil skeleton under the impact of water flow. Therefore, the stress variation within the soil remains relatively small during this initial stage. In the vertical direction during the initial stage, disturbances are greater the closer they are to the pipeline defect, and the duration of disturbance is longer.

During the erosion stage, there is a short-term intense stress drop phenomenon. In the vertical directions H_1 , H_2 , H_3 , H_4 , and H_5 , stress decreases by 8.04 kPa, 14.06 kPa, 13.15 kPa, 7.13 kPa, and 3.53 kPa respectively within 2.59 s. In the later part of this stage, the stress evolution curves gradually rise and stabilize. It can be observed that during this stage, seepage force gradually exceeds the maximum restraint force of the coarse particles constituting the soil skeleton, leading to movement of soil particles. At this point, the soil skeleton is eroded, causing structural damage to the soil, and forming cavities near the pipeline defect. The cohesion between sand particles in the stratum is low, allowing cavities to develop rapidly. It is observed that the top cylindrical area of the cavity suddenly sinks, briefly forming a cylindrical collapse pit. The closer the upper stratum and the pipeline defect are during this stage, the more pronounced the collapse erosion, and the faster the stress response.

During the early stable stage from 1250 to 2000s, the curve shows slight fluctuations. The overlying soil undergoes instability due to seepage, resulting in sand flow phenomena and the formation of regular conical collapse pit that slowly expand. In the late stable stage, complete collapse development occurs, and collapse stabilizes. At this point, the stresses at H_1 , H_2 , H_3 , H_4 , and H_5 are -9.24 kPa, -13.67 kPa, -11.72 kPa, -5.33 kPa, and -1.58 kPa respectively. It can be seen that at this stage, collapse is complete, and there is still sand covering the pipeline defect, measuring 22.01 cm (Fig. 8). H_1 , located near the defect, shows relatively minor stress variations under the overlying sand and seepage effect.

From the vertical stress evolution curve, it is observed that in the initial stage, there is minimal stress variation at each monitoring point, and the evolution curve is convex-shaped. At this point, the pipeline leakage has just begun, and the seepage force acting on the coarse particle skeleton of the soil is insufficient to induce particle movement; thus, the soil above the pipeline defect remains stable. During the erosion stage, a significant stress drop occurs. By 370 s into the test, the stress distribution at points H_1 , H_2 , H_3 , H_4 , and H_5 has noticeably changed, with collapse cavities appearing above the pipeline defect. During this stage, the seepage forces are sufficient to mobilize coarse particles, leading to soil structural damage. In the stable stage, the stress curve shows slight fluctuations. During this period, the stress decreases in the overlying soil above the pipeline defect, and collapse develops laterally, accompanied by sand flow phenomena. Collapse development completes during this stage, and there remains a 22.01 cm sand covering the pipeline defect. It is evident that the closer the location is to the pipeline defect, the more severe the erosion, the greater the disturbance amplitude, and the longer the disturbance duration.

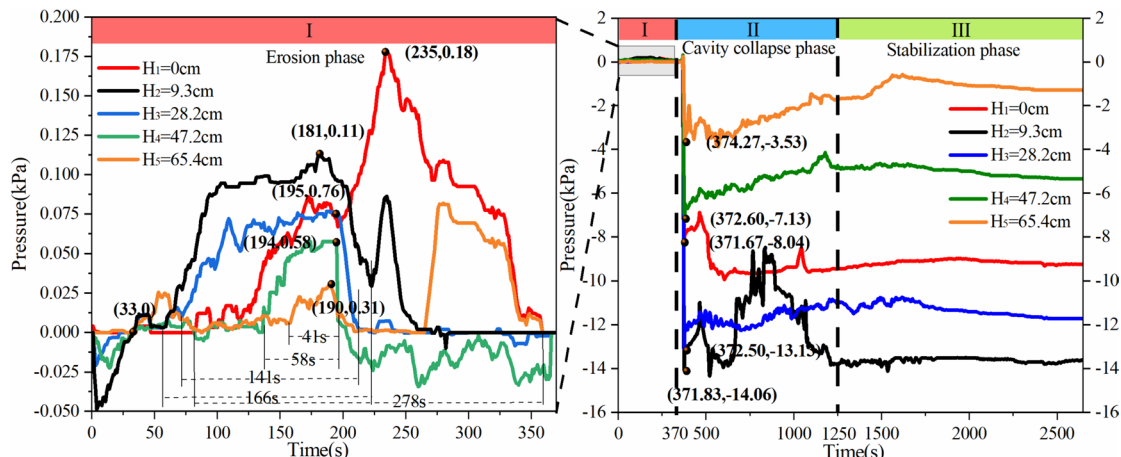


Figure 7. Stress evolution in the vertical direction.

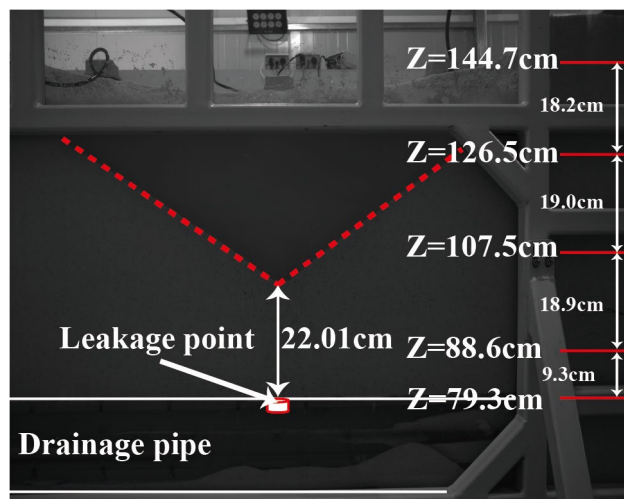


Figure 8. Different strata division.

Analysis and discussion of stress evolution in the horizontal direction

It has been observed from previous experiments^{46,47} that most collapses caused by pipeline leakage exhibit conical or cylindrical shapes. In order to investigate the water-soil interaction during the collapse process and the evolution of horizontal stresses, this test deployed 5 layers of soil pressure sensors arranged in a conical distribution. According to the experimental results, the first group consists of 2 layers with 8 sensors positioned between the pipeline defect and the bottom of the conical collapse pit, with overlying sand of 22.01 cm and 12.71 cm respectively. The second group comprises 3 layers with 17 sensors positioned above the collapse pit, at distances of 6.19 cm, 25.19 cm, and 43.39 cm from the bottom of the conical collapse pit, as shown in Fig. 8. Considering that the center point sensors in each layer horizontally align with the vertical sensors, the test is still divided into initial stage (0–370 s), erosion stage (371–1250 s), and stable stage (1251–2648 s) to analyze the horizontal stress variations and water-soil interactions.

Analysis of horizontal stress evolution in the formation below the collapse

The sensors in the first group are positioned at heights of $Z=79.3$ cm and $Z=88.6$ cm respectively, as shown in Fig. 9. The distribution of sensors forms a semicircle centered at the collapse centers CH3 and CH8, with radii of 14 cm and 20 cm respectively. The horizontal soil stress evolution at $Z=79.3$ cm is depicted in Fig. 10, where it can be observed that the stress evolution at the collapse centers aligns with the curve at point H_1 from Section "Analysis and discussion of stress evolution in the vertical direction". The stress evolution trends at points L_1 and L_2 on the circle are largely consistent, while L_3 shows slight differences. At L_1 and L_2 , the stress slowly changes in the initial stage, displaying a convex curve. At 235 s, the maximum stress reaches 0.18 kPa and stabilizes at 1.41 kPa and 1.07 kPa in the second and third stages respectively. At L_3 , the stress remains constant at 0 kPa in

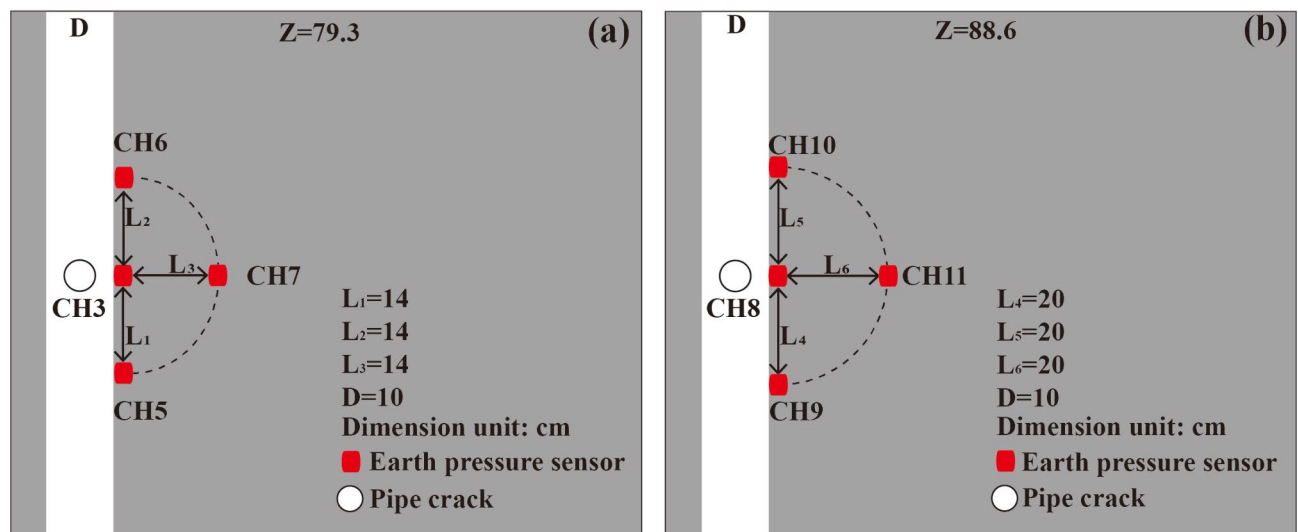


Figure 9. Distribution of horizontal sensors in the first group.

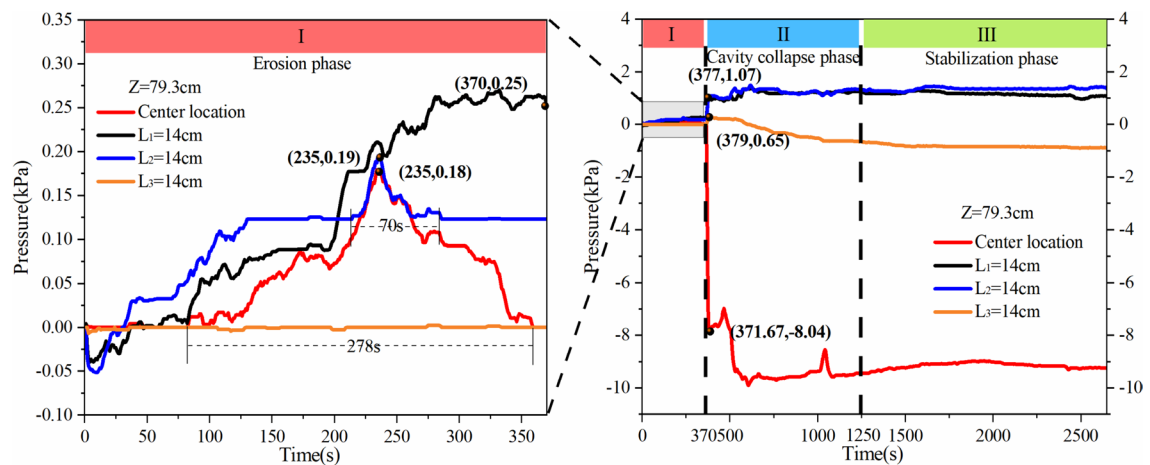


Figure 10. Stress evolution in the $Z=79.3$ cm stratum.

the first stage, decreases by 0.64 kPa in the second stage, and stabilizes at -0.88 kPa in the third stage, with the stress drop being only 9.52% of that at the center points. The sensors at $Z=79.3$ cm are horizontally aligned with the pipeline defect, and considering the conical shape of the collapse pit, stress variations are primarily influenced by the thickness of the overlying soil. Hence, the stress drop occurs at L_3 . Meanwhile, at L_1 and L_2 , due to their proximity to the model boundaries, boundary effects are significant, resulting in minor stress increases under seepage effects in the overlying strata.

The horizontal soil stress evolution at $Z=88.6$ cm is depicted in Fig. 11. It can be observed that in the first stage, the evolution trends at L_4 , L_5 , and L_6 are largely consistent with those at L_1 , L_2 , and L_3 at $Z=79.3$ cm. Specifically, the curve at L_6 remains stable, while L_4 and L_5 exhibit convex-shaped curves in the first stage, reaching peak values of 0.08 kPa and 0.10 kPa at 237 s respectively. At the beginning of the second stage, L_4 , L_5 , and L_6 show rapid increases followed by gradual decreases. Notably, L_6 experiences the largest stress drop, reaching -2.39 kPa, which is 13.61% of the stress drop at the center points. Despite the presence of overlying sand at both $Z=79.3$ cm and $Z=88.6$ cm, the soil stress variations are more pronounced at $Z=88.6$ cm at the same positions. Considering the closer proximity of $Z=88.6$ cm to the collapse pit, it experiences greater influence from the loss of overlying soil particles and more severe erosion. In strata between the pipeline defect and the bottom of the conical collapse pit, closer proximity to the defect results in less pronounced effects. The strata continue to be covered by sand despite the pipeline leakage, primarily affected by the loss and seepage of overlying soil particles during the leakage process.

Analysis of the horizontal stress evolution in the stratum above the collapse

The sensors in the second group are positioned at heights of $Z=107.5$ cm, $Z=126.5$ cm, and $Z=144.7$ cm respectively, as shown in Fig. 12. These sensors are located above the bottom of the collapse pit and are arranged in a semi-circular pattern. At $Z=107.5$ cm, there are 4 sensors oriented around the center point CH12 of the collapse, with a radius of 25 cm. At $Z=126.5$ cm, there are 7 sensors arranged in a double semi-circular pattern around the center point CH26, with radii of 25 cm and 40 cm. At $Z=144.7$ cm, there are 6 sensors also arranged in a double semi-circular pattern around the center point CH39, with radii of 25 cm and 50 cm.

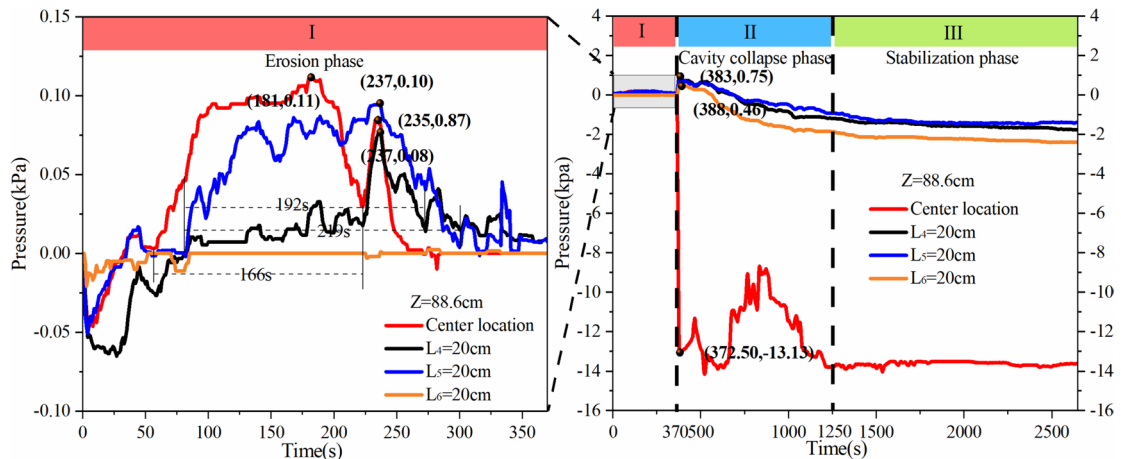


Figure 11. Stress evolution in the $Z=88.6$ cm stratum.

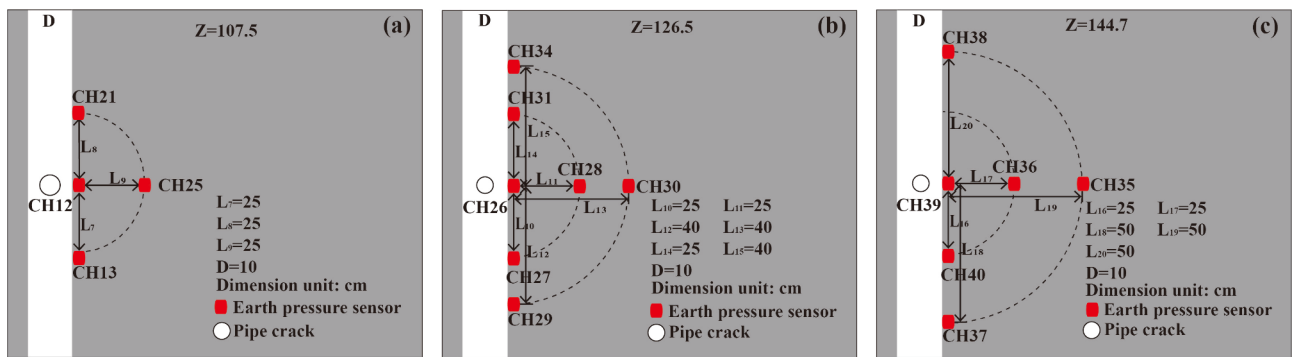


Figure 12. Distribution of horizontal sensors in the second group.

The horizontal soil stress evolution at $Z = 107.5$ cm is shown in Fig. 13. It is evident that the stress evolution trends at L_7 , L_8 , and L_9 are nearly identical. In the initial stage, the stress curves show minor fluctuations. Around 390 s in the erosion stage, the stress curves rise sharply, reaching a maximum increase of 0.81 kPa, followed by a gradual decrease, which is markedly different from the rapid stress drop observed at the center point CH12. In the third stage, the three stress curves gradually stabilize at a mean value of 6.60 kPa, with an average stress drop of 56.31% compared to the center point. The soil pressure sensors at $Z = 107.5$ cm are positioned just above the bottom of the collapse pit, 6.19 cm away, where saturated sand migrates into the pipeline under erosion, leading to significant loss of the overlying sand. Compared to the evolution of stress curves at the bottom of the collapse pit in the first group, the upper strata above the collapse bottom experience greater disturbance.

The horizontal stress evolution at $Z = 126.5$ cm is analyzed with radii of 25 cm and 40 cm, as shown in Fig. 14. Compared to the horizontal stress evolution at $Z = 107.5$ cm with a radius of 25 cm, the stress evolution within this stratum closely resembles that at the central point. It can be observed that L_{10} , L_{11} , and L_{14} experience significant stress drops during the erosion phase at 415 s, 599 s, and 594 s respectively, stabilizing in the stable phase at -5.29 kPa. The average stress drop is 99.25% of the central stress drop. When $R = 40$ cm within this stratum, L_{12} , L_{13} , and L_{15} show stress drops occurring later in the erosion phase, at 433 s, 598 s, and 813 s respectively. In the stable phase, the three stress curves stabilize at -5.29 kPa, -3.00 kPa, and -5.29 kPa, with an average stress drop of 84.99% compared to the central stress drop. It is evident that within the same stratum, the collapse develops outward from the central point. Based on the horizontal stress evolution with radii of 25 cm at $Z = 107.5$ cm and $Z = 126.5$ cm, it is known that closer proximity to the surface results in a slower disturbance and less erosion within the collapse pit. Additionally, comparing the horizontal stress evolution between radii of 25 cm and 40 cm at $Z = 126.5$ cm indicates that erosion slows with increased distance from the collapse center within the same stratum. In summary, the collapse exhibits a conical distribution from the bottom to the surface, with the collapse progressing outward from the center to the periphery within the same stratum.

The horizontal stress evolution at $Z = 144.7$ cm is analyzed with radii of 25 cm and 50 cm, as shown in Fig. 15. For $R = 25$ cm, the horizontal stress at L_{16} and L_{17} shows stress drops at 499 s and 600 s during the second stage, respectively, and stabilizes at -0.65 kPa and -2.47 kPa in the third stage, which is 84.81% of the central stress drop. Within this stratum, for $R = 50$ cm, the stress curves at L_{18} , L_{19} , and L_{20} show stress drops at 921 s, 1017 s, and 1062 s, respectively, and exhibit significant fluctuations after the drop, eventually reaching -5.56 kPa, -0.12 kPa, and 1.08 kPa, showing notable differences. The $Z = 144.7$ cm stratum is only covered by a 14.6 cm sand, indicating that erosion occurs relatively slowly compared to the lower stratum and is less intense. Considering the

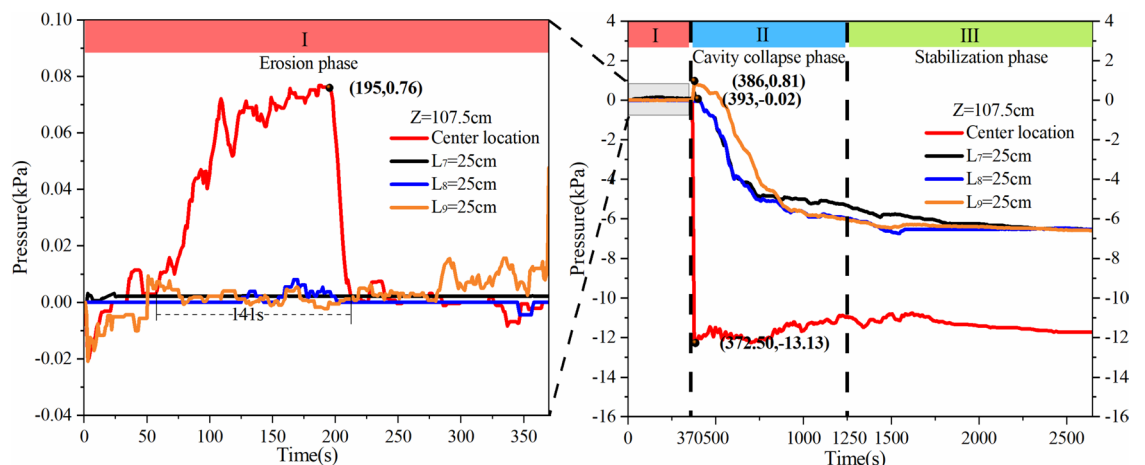
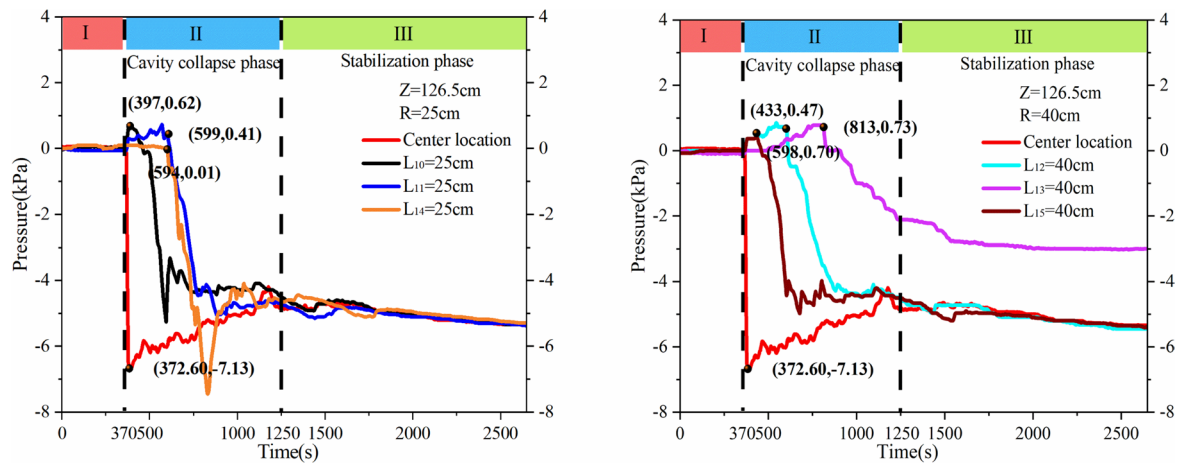
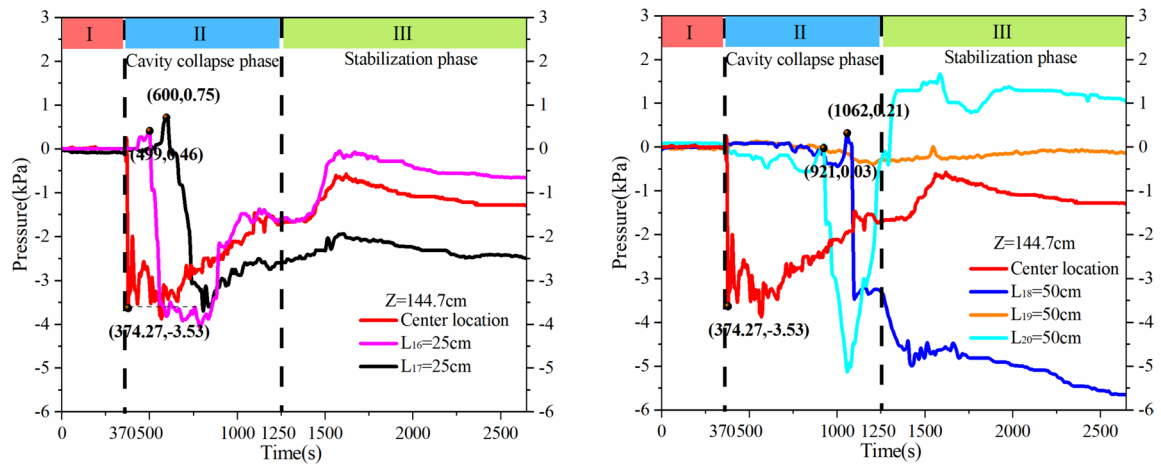


Figure 13. Stress evolution in the $Z = 107.5$ cm stratum.

**Figure 14.** Stress evolution in the $Z = 126.5$ cm stratum.**Figure 15.** Stress evolution in the $Z = 144.7$ cm stratum.

proximity of this stratum to the surface, erosion during leakage leads to significant displacement of the stratum. After the test, it was observed that most sensors within the $R = 50$ cm radius in this stratum were displaced or tilted, resulting in severe fluctuations in the stress evolution curves.

From the horizontal stress evolution curves of different strata mentioned above, it can be seen that during the leakage process, the collapse develops from the central point outward, forming a regular conical distribution that erodes the soil stratum. Observing the stress curves within the first and second groups of soil strata, it is evident that the stress evolution trends differ entirely between the strata at the bottom of the collapse pit and those above the pit. The soil at the bottom of the collapse pit is primarily affected by the loss of the overlying soil and seepage, resulting in slow changes in the stress curve and a relatively small stress drop. The difference in stress evolution compared to the central point is significant, with the average stress drop being 9.52% and 13.61% of the central point. It can be concluded that when pipeline leakage occurs, the soil beneath the conical collapse pit is less affected as the distance from the bottom of the collapse pit increases. The soil above the collapse pit, where the overlying saturated sand migrates to the pipeline under erosion, experiences severe erosion. Its stress evolution curve closely matches that of the central point, with stress drops stabilizing at above 55%, and it shows a trend of being higher in the middle and lower on both sides. The results indicate that for the soil above the pit, the closer they are to the surface, the slower the disturbance and the less erosion they experience; horizontally within the same stratum, the farther from the collapse center point, the slower the erosion and the lesser the disturbance.

Analysis and discussion of the collapse process

The collapse caused by pipeline leakage typically occurs underground at considerable depths, making it difficult to observe soil particle displacement with the naked eye, especially in the initial stages of leakage. To address this, DIC technology were employed. By capturing grayscale digital images of the side surface of the sandy soil and comparing and analyzing the changes in these images over time, the deformation and displacement of soil particles were monitored, and the results are shown in Fig. 16. In Fig. 16, the orange background represents the calculation area, and the white lines represent the interface where particle movement occurs, with darker colors indicating greater displacement. It can be seen that before the initial stage of leakage (370 s), the seepage force is

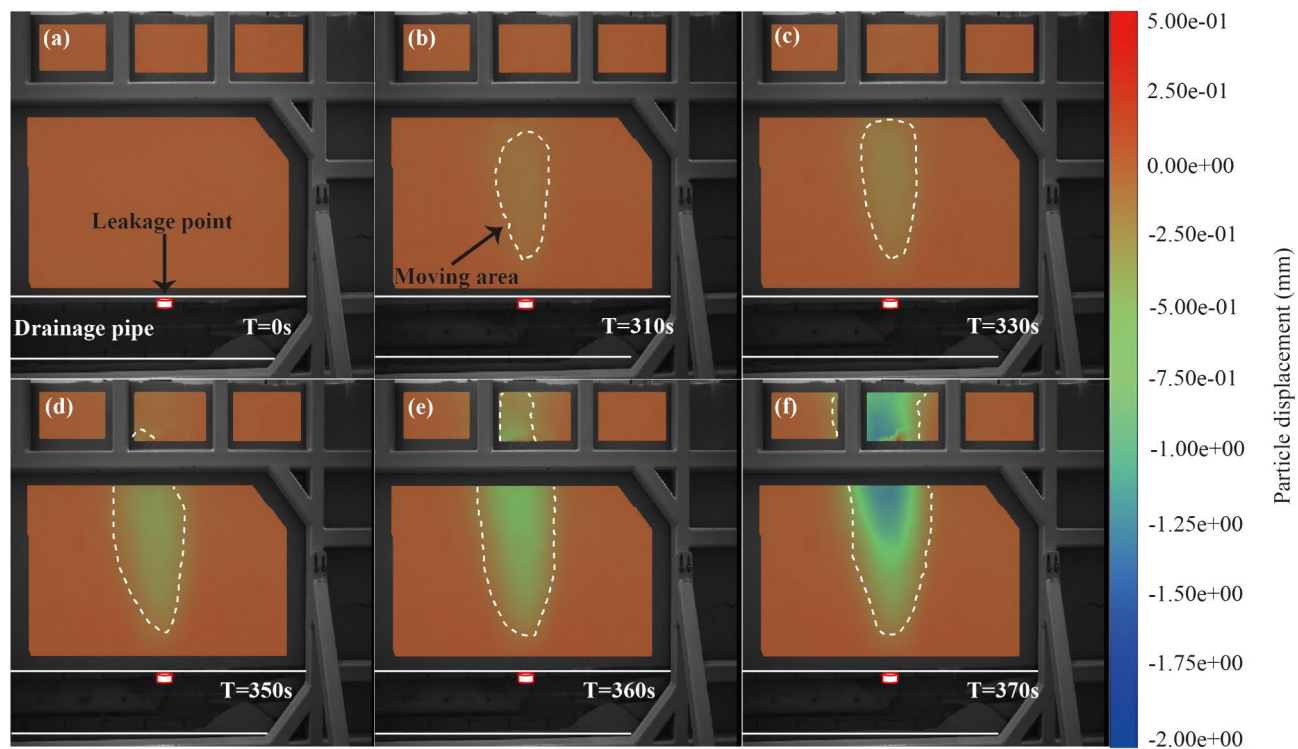


Figure 16. Transportation of soil particles during collapse.

insufficient to cause the soil particle skeleton to break, resulting in the loss of fine particles with little observable displacement. As the seepage force gradually exceeds the maximum restraint force of the soil skeleton, the coarse particle skeleton is lost, the soil structure is damaged, and cavities form inside the pipeline, quickly developing upwards until the top subsides (Fig. 16b-f).

As the loss of sandy soil at the top occurs, the pipeline leakage enters the collapse pit development stage, as shown in Fig. 17. In Fig. 17, the red lines represent the shape of the collapse pit development. During this stage, the soil coarse particle skeleton continues to be destroyed, the internal cavity of the formation gradually expands to the surface, and a cylindrical subsidence suddenly forms in the cylindrical area at the surface. In Fig. 17b, an irregular concave collapse initially appears at the top. As leakage worsens, the collapse pit's shoulder collapses (Fig. 17c-e). As the overlying stratum is eroded and damaged, sandy soil is lost from both sides, and the shape of the collapse pit gradually develops into a regular cone, exhibiting significant progressive characteristics (Fig. 17f-h). It is evident that the shape of the collapse pit changes rapidly in the early stages of development.

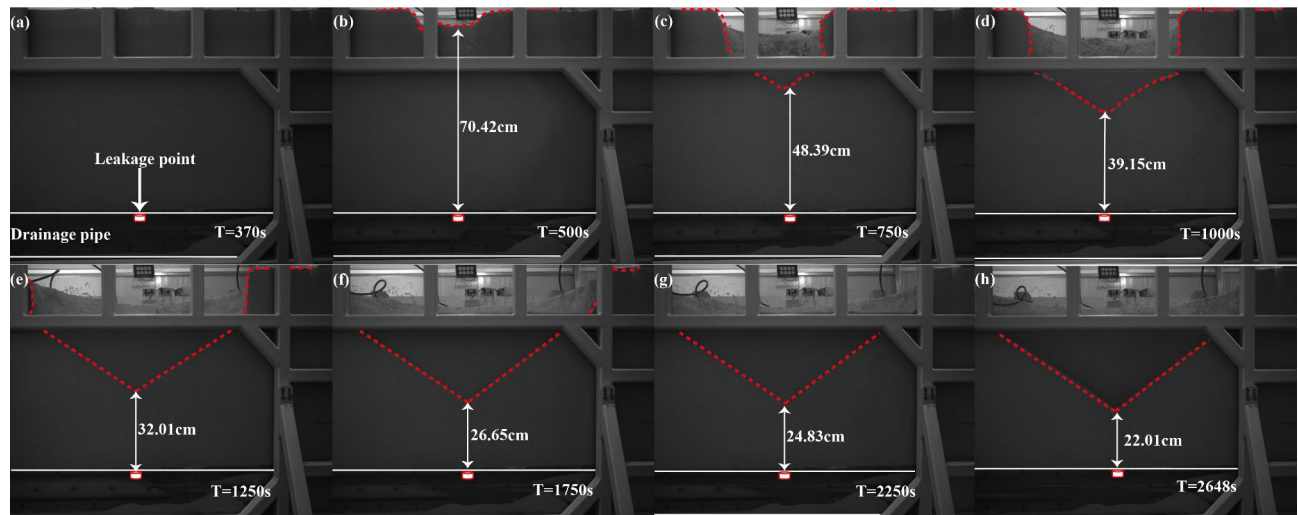


Figure 17. Collapse development.

With the appearance of flow sand phenomena at the shoulders, the collapse pit development completes, and the expansion speed slows down.

The experimental results indicate that the seepage effect of groundwater plays a crucial role in ground collapse caused by pipeline leakage. When the seepage force is relatively small, it is insufficient to damage the coarse particle skeleton, and the soil remains stable. However, as the seepage force increases and exceeds the maximum restraint force of the coarse particle skeleton, erosion occurs, and the soil structure is compromised. With continued increase in seepage force, the overlying soil layer becomes unstable due to erosion, leading to collapse. In the process of ground collapse induced by erosion from pipeline leakage, groundwater seepage provides the driving force for the collapse of the soil. This seepage, along with the transport space created by the defect, jointly promotes the occurrence of ground collapse.

Conclusions

This study investigates the mechanism of soil collapse due to pipeline leakage through physical model test. It provides a detailed report on the stress evolution and collapse characteristics of soil stratum in different directions under leakage conditions and analyzes the internal soil erosion process within the strata. Additionally, the study combines sensor measurements and DIC technology to discuss the soil–water interaction mechanisms within the soil layers. The results indicate:

1. Groundwater seepage during pipeline leakage provides the driving force for the collapse of geotechnical bodies. When the seepage force is small, it is insufficient to cause damage to the coarse particle skeleton, and the soil remains stable. However, when the seepage force increases beyond the maximum constraint of the coarse particle skeleton, the skeleton is eroded, leading to the destruction of the soil structure. It can be observed that groundwater seepage acts as the driving force for the collapse and, together with the migration space provided by the defect, leads to ground collapse.
2. The stress evolution of soil during pipeline leakage is closely related to the height of the conical collapse pit. Below the collapse pit, the soil primarily experience slow stress changes due to the loss of the overlying sand and seepage effects, resulting in minimal erosion. Above the collapse pit, saturated sand migrates into the pipeline under erosive forces, leading to rapid stress changes and significant erosion.
3. In the vertical direction, the stress drop decreases as the distance from the bottom of the conical collapse increases. At stratum heights of 79.3 cm, 88.6 cm, 107.5 cm, 126.5 cm, and 144.7 cm, the stress drops at the center points above the defect opening are -9.24 kPa , -13.67 kPa , -11.72 kPa , -5.33 kPa , and -1.58 kPa , respectively.
4. In the horizontal direction, as the distance from the collapse center increases, the erosion rate decreases. The average stress drops within the same layer are 9.52%, 13.61%, 56.31%, 99.25%, and 84.81% of the central stress drop, respectively.
5. During the initial stage of collapse development, the internal cavity changes rapidly. As the phenomenon of sand flow from the shoulder occurs, the collapse development completes, the expansion speed slows down, and the collapse ultimately takes on a regular conical shape.

Currently, the impact of collapse pit height on subsidence due to buried pipeline leakage and soil erosion has not been thoroughly studied. However, experimental results indicate that the stress evolution in soil above and below the collapse pit bottom is significantly different, potentially offering insights for predicting subsidence caused by buried pipeline leakage. Future research will focus on the factors influencing collapse pits and their correlation with erosion.

Data availability

The datasets generated and/or analysed during the current study are not publicly available due to the need for follow-up studies but are available from the corresponding author on reasonable request.

Received: 23 April 2024; Accepted: 29 July 2024

Published online: 31 July 2024

References

1. Momeni, A., Piratla, K. R., Anderson, A., Madathil, K. C. & Li, D. Stochastic model-based leakage prediction in water mains considering pipe condition uncertainties. *Tunn. Undergr. Space Technol.* <https://doi.org/10.1016/j.tust.2023.105130> (2023).
2. Sun, W. *et al.* Real-time observation of meso-fracture process in backfill body during mine subsidence using X-ray CT under uniaxial compressive conditions. *Constr. Build. Mater.* **113**, 153–162. <https://doi.org/10.1016/j.conbuildmat.2016.03.050> (2016).
3. Reda, A., Mahmoud, R. M. A., Shahin, M. A., Amaechi, C. V. & Sultan, I. A. Roadmap for recommended guidelines of leak detection of subsea pipelines. *J. Mar. Sci. Eng.* <https://doi.org/10.3390/jmse12040675> (2024).
4. Parise, M. The impacts of quarrying in the Apulian Karst (Italy). *Adv. Res. Karst Media* https://doi.org/10.1007/978-3-642-12486-0_68 (2010).
5. Chaussard, E., Amelung, F., Abidin, H. & Hong, S. H. Sinking cities in Indonesia: ALOS PALSAR detects rapid subsidence due to groundwater and gas extraction. *Remote Sens. Environ.* **128**, 150–161. <https://doi.org/10.1016/j.rse.2012.10.015> (2013).
6. Rahnema, H. & Mirasi, S. Seismic and geotechnical study of land subsidence and vulnerability of rural buildings. *Int. J. Geosci.* **3**, 878–884. <https://doi.org/10.4236/ijg.2012.324089> (2012).
7. Rasol, M. *et al.* GPR monitoring for road transport infrastructure: A systematic review and machine learning insights. *Constr. Build. Mater.* <https://doi.org/10.1016/j.conbuildmat.2022.126686> (2022).
8. Wang, X.-W. & Xu, Y.-S. Investigation on the phenomena and influence factors of urban ground collapse in China. *Nat. Hazards* **113**, 1–33. <https://doi.org/10.1007/s11069-022-05304-z> (2022).

9. Zhang, D.-M., Du, W.-W., Peng, M.-Z., Feng, S.-J. & Li, Z.-L. Experimental and numerical study of internal erosion around submerged defective pipe. *Tunn. Undergr. Space Technol.* <https://doi.org/10.1016/j.tust.2019.103256> (2020).
10. Kuwano, R., Horii, T., Yamauchi, K. & Kohashi, H. Formation of subsurface cavity and loosening due to defected old sewer pipe. *Jpn. Geotech. J.* **5**, 349–361. <https://doi.org/10.3208/jgs.5.349> (2010).
11. Zhou, H. T., Liu, C. Q., Wang, G. H., Kang, K. & Liu, Y. H. Study on drilling ground collapse induced by groundwater flow and prevention based on a coupled CFD-DEM method. *KSCE J. Civ. Eng.* **26**, 2112–2125. <https://doi.org/10.1007/s12205-022-1061-x> (2022).
12. Mirassi, S. & Rahnema, H. Deep cavity detection using propagation of seismic waves in homogenous half-space and layered soil media. *Asian J. Civil Eng.* **21**, 1431–1441. <https://doi.org/10.1007/s42107-020-00288-2> (2020).
13. Kim, K., Kim, J., Kwak, T.-Y. & Chung, C.-K. Logistic regression model for sinkhole susceptibility due to damaged sewer pipes. *Nat. Hazards* **93**, 765–785. <https://doi.org/10.1007/s11069-018-3323-y> (2018).
14. Bertrand-Krajewski, J.-L. *et al.* Towards a better knowledge and management of infiltration and exfiltration in sewer systems: The APUSS project. *Water Pract. Technol.* **1**, wpt2006021. <https://doi.org/10.2166/wpt.2006.021> (2006).
15. Kwon, Y.-M., Moon, J.-H., Cho, G.-C., Kim, Y.-U. & Chang, I. Xanthan gum biopolymer-based soil treatment as a construction material to mitigate internal erosion of earthen embankment: A field-scale. *Construct. Build. Mater.* <https://doi.org/10.1016/j.conbuildmat.2023.131716> (2023).
16. Karpf, C., Hoeft, S., Scheffer, C., Fuchs, L. & Krebs, P. Groundwater infiltration, surface water inflow and sewerage exfiltration considering hydrodynamic conditions in sewer systems. *Water Sci. Technol.* **63**, 1841–1848. <https://doi.org/10.2166/wst.2011.388> (2011).
17. Balkaya, M., Moore, I. D. & Saglamer, A. Study of non-uniform bedding due to voids under jointed PVC water distribution pipes. *Geotext. Geomembr.* **34**, 39–50. <https://doi.org/10.1016/j.geotexmem.2012.01.003> (2012).
18. Fenner, R. A. Influence of sewer bedding arrangements on infiltration rates on soil migration. *Municipal Engineer (Institution of Civil Engineers)*, Vol. **8**, 105 (1991).
19. Karoui, T., Jeong, S.-Y., Jeong, Y.-H. & Kim, D.-S. Experimental study of ground subsidence mechanism caused by sewer pipe cracks. *Appl. Sci.-Basel*. <https://doi.org/10.3390/app8050679> (2018).
20. Chang, D. & Zhang, L. Extended internal stability criteria for soils under seepage. *Soils Found.* **53**, 569. <https://doi.org/10.1016/j.sandf.2013.06.008> (2013).
21. Ben-Mansour, R., Habib, M. A., Khalifa, A., Youcef-Toumi, K. & Chatzigeorgiou, D. Computational fluid dynamic simulation of small leaks in water pipelines for direct leak pressure transduction. *Comput. Fluids* **57**, 110–123. <https://doi.org/10.1016/j.compfluid.2011.12.016> (2012).
22. Ibrahim, A. & Meguid, M. A. CFD-DEM simulation of sand erosion into defective gravity pipes under constant groundwater table. *Tunn. Undergr. Space Technol.* <https://doi.org/10.1016/j.tust.2022.104823> (2023).
23. Peche, A., Graf, T., Fuchs, L. & Neuweiler, I. A coupled approach for the three-dimensional simulation of pipe leakage in variably saturated soil. *J. Hydraul.* **555**, 569–585. <https://doi.org/10.1016/j.jhydrol.2017.10.050> (2017).
24. Qi, G. *et al.* Analysis of instability mechanism and induced cause of urban pavement in Xining City, China. *Adv. Mater. Sci. Eng.* <https://doi.org/10.1155/2022/3365402> (2022).
25. Cheng, K., Wang, Y. & Yang, Q. A semi-resolved CFD-DEM model for seepage-induced fine particle migration in gap-graded soils. *Comput. Geotech.* **100**, 30–51. <https://doi.org/10.1016/j.compgeo.2018.04.004> (2018).
26. Cui, X., Li, J., Chan, A. & Chapman, D. Coupled DEM-LBM simulation of internal fluidisation induced by a leaking pipe. *Powder Technol.* **254**, 299–306. <https://doi.org/10.1016/j.powtec.2014.01.048> (2014).
27. Al-Halbouni, D. *et al.* Geomechanical modelling of sinkhole development using distinct elements: Model verification for a single void space and application to the Dead Sea area. *Solid Earth* **9**, 1341–1373. <https://doi.org/10.5194/se-9-1341-2018> (2018).
28. Tang, Y., Chan, D. H. & Zhu, D. Z. A coupled discrete element model for the simulation of soil and water flow through an orifice. *Int. J. Numer. Anal. Methods Geomech.* **41**, 1477–1493. <https://doi.org/10.1002/nag.2677> (2017).
29. Van Zyl, J. E. & Cassa, A. M. Modeling elastically deforming leaks in water distribution pipes. *J. Hydraul. Eng.* **140**, 182–189. [https://doi.org/10.1061/\(asce\)hy.1943-7900.0000813](https://doi.org/10.1061/(asce)hy.1943-7900.0000813) (2014).
30. Cui, X., Li, J., Chan, A. & Chapman, D. A 2D DEM-LBM study on soil behaviour due to locally injected fluid. *Particuology* **10**, 242–252. <https://doi.org/10.1016/j.partic.2011.10.002> (2012).
31. Ali, H. & Choi, J.-h. Risk prediction of sinkhole occurrence for different subsurface soil profiles due to leakage from underground sewer and water pipelines. *China Civil Eng J* **12**, 310. <https://doi.org/10.3390/su12010310> (2020).
32. Mukunoki, T., Kumano, N., Otani, J. & Kuwano, R. Visualization of three dimensional failure in sand due to water inflow and soil drainage from defective underground pipe using X-ray CT. *Soils Found.* **49**, 959–968. <https://doi.org/10.3208/sandf.49.959> (2009).
33. Ke, L. & Takahashi, A. Triaxial erosion test for evaluation of mechanical consequences of internal erosion. *Geotech. Test. J.* **37**, 347–364 (2014).
34. Indiketiya, S., Jegatheesan, P. & Rajeev, P. Evaluation of defective sewer pipe-induced internal erosion and associated ground deformation using laboratory model test. *Can. Geotech. J.* **54**, 1184–1195. <https://doi.org/10.1139/cgj-2016-0558> (2017).
35. Walski, T., Bezts, W., Poslusny, E. T., Weir, M. & Whitman, B. E. Modeling leakage reduction through pressure control. *J. Am. Water Works Assoc.* **98**, 147–155 (2006).
36. Sato, M. & Kuwano, R. Influence of location of subsurface structures on development of underground cavities induced by internal erosion. *Soils Found.* **55**, 829–840. <https://doi.org/10.1016/j.sandf.2015.06.014> (2015).
37. Zhang, C., Yue, Y. & Wang, M. Influence of pipeline leakage on ground collapse and its control during adjacent tunnelling. *China Civil Eng. J.* **48**, 351–356 (2015).
38. Guo, S., Shao, Y., Zhang, T. Q., Zhu, D. Z. & Zhang, Y. P. Physical modeling on sand erosion around defective sewer pipes under the influence of groundwater. *J. Hydraul. Eng.* **139**, 1247–1257. [https://doi.org/10.1061/\(asce\)hy.1943-7900.0000785](https://doi.org/10.1061/(asce)hy.1943-7900.0000785) (2013).
39. Cui, X. L., Tao, G. L., Li, J. & Iop. In *2nd International Workshop on Renewable Energy and Development (IWRD)* (2018).
40. Sato, M. & Kuwano, R. *Model tests for the evaluation of formation and expansion of a cavity in the ground* (Deren of Civi Engineering, The University of Tokyo, JnInsiue of Indusri Science, The Universiy of Tokyo, Jn, 2010).
41. Mukunoki, T., Kumano, N. & Otani, J. Image analysis of soil failure on defective underground pipe due to cyclic water supply and drainage using X-ray CT. *Front. Struct. Civil Eng.* **6**, 85–100. <https://doi.org/10.1007/s11709-012-0159-5> (2012).
42. Tan, Y. & Lu, Y. Forensic diagnosis of a leaking accident during excavation. *J. Perform. Construct. Facil.* [https://doi.org/10.1061/\(asce\)cf.1943-5509.0001058](https://doi.org/10.1061/(asce)cf.1943-5509.0001058) (2017).
43. Wang, Y., Shi, G., Tian, X., Li, C. & Cheng, H. Experimental study on city road collapse under vibrating load. *Shock Vib.* **1–13**, 2020. <https://doi.org/10.1155/2020/6074658> (2020).
44. Tan, F. *et al.* Model test analysis of subsurface cavity and ground collapse due to broken pipe leakage. *Appl. Sci.* **12**, 13017. <https://doi.org/10.3390/app122413017> (2022).
45. Zoueshtiagh, F. & Merlen, A. Effect of a vertically flowing water jet underneath a granular bed. *Phys. Rev. E.* <https://doi.org/10.1103/PhysRevE.75.056313> (2007).
46. van Zyl, J. E., Alsaydalani, M. O. A., Clayton, C. R. I., Bird, T. & Dennis, A. Soil fluidisation outside leaks in water distribution pipes—preliminary observations. *Proc. Inst. Civil Eng. Water Manag.* **166**, 546–555. <https://doi.org/10.1680/wama.11.00119> (2013).
47. Alsaydalani, M. O. A. & Clayton, C. R. I. Internal fluidization in granular soils. *J. Geotech. Geoenviron. Eng.* [https://doi.org/10.1061/\(asce\)gt.1943-5606.0001039](https://doi.org/10.1061/(asce)gt.1943-5606.0001039) (2014).

Acknowledgements

This work was supported by the Geological survey project, China Geological Survey (Numbers: 20221732, 20230116).

Author contributions

J.G.: Conceptualization, Methodology, Writing—original draft, Formal analysis, Validation. Y.Z.: Conceptualization, Methodology, Writing—review & editing. Y.L.: Conception, Analysis, Methodology. X.Z.: Conception, Analysis, Methodology. J.Z.: Methodology, Investigation. H.S.: Analysis. Q.Z.: Investigation. Z.C.: Methodology. Y.M.: Conceptualization.

Competing interests

The authors declare no competing interests.

Additional information

Correspondence and requests for materials should be addressed to Y.Z.

Reprints and permissions information is available at www.nature.com/reprints.

Publisher's note Springer Nature remains neutral with regard to jurisdictional claims in published maps and institutional affiliations.



Open Access This article is licensed under a Creative Commons Attribution-NonCommercial-NoDerivatives 4.0 International License, which permits any non-commercial use, sharing, distribution and reproduction in any medium or format, as long as you give appropriate credit to the original author(s) and the source, provide a link to the Creative Commons licence, and indicate if you modified the licensed material. You do not have permission under this licence to share adapted material derived from this article or parts of it. The images or other third party material in this article are included in the article's Creative Commons licence, unless indicated otherwise in a credit line to the material. If material is not included in the article's Creative Commons licence and your intended use is not permitted by statutory regulation or exceeds the permitted use, you will need to obtain permission directly from the copyright holder. To view a copy of this licence, visit <http://creativecommons.org/licenses/by-nc-nd/4.0/>.

© The Author(s) 2024